Journal of Materials Chemistry C

ROYAL SOCIETY OF CHEMISTRY

PAPER

View Article Online
View Journal | View Issue

Cite this: J. Mater. Chem. C, 2025, 13, 15168

Impact of thermally activated ionic dynamics on the trap-mediated current–voltage characteristics of a mixed-halide hybrid perovskite†

Manoj Singh,[a] Lokesh Singh Tanwar[a] and Rupak Banerjee *[ab]

Organic–inorganic metal halide perovskites (OIMHPs) are at the forefront of leading energy research. Therefore, it is pivotal to understand the effect of operating conditions like temperature, humidity, light exposure, *etc.* on these materials. The transient ionic dynamics and its effect on the steady-state *J*–*V* characteristics of an OIMHP, *viz.* $FAPbBr_2I$, having a mixed halide composition, were investigated by temperature-dependent dielectric spectroscopy and temperature-dependent space charge limited current (SCLC) measurements in the temperature range of 305–454 K. The contribution of the resistance and capacitance of grains and grain boundaries to the total impedance at different temperatures has been interpreted by analyzing the Bode plots using the Maxwell–Wagner equivalent circuit model. The AC conductivity spectra demonstrate different behaviors in two different temperature regimes. In the low-temperature (LT) regime (323–381 K), the temperature response of ionic conductivity is only dependent on hopping frequency (the ionic carrier concentration factor being temperature-independent), leading to almost similar activation energies of ionic conduction (E_a) and hopping migration (E_m), where $E_a = E_m = 0.30 \pm 0.05$ eV. However, in the high temperature (HT) regime (395–454 K), we observed a difference in E_a (0.74 ± 0.05 eV) and E_m (0.50 ± 0.05 eV) values, which is attributed to the activation energy of mobile charge carrier formation ($E_f = E_a - E_m = 0.24 \pm 0.05$ eV). We propose that the trapped ions in the LT regime are now released by overcoming the barrier E_f in the HT regime, leading to a substantial increase in the mobile ion concentration. Furthermore, we have unveiled the effect of these mobile ions and trapped carriers on the *J*–*V* characteristics in both temperature regimes by analyzing the temperature-dependent SCLC *J*–*V* characteristics in the Ag/$FAPbBr_2I$/Ag device configuration. The AC conductivity and electric modulus loss spectra scale to different master curves in the LT and HT regimes, further corroborating the observed thermally activated interplay of ionic conduction and hopping migration. The key findings of this work stimulate more such fundamental investigations of electrical transport in mixed halide OIMHPs and establish their potential in various energy storage applications like batteries, integrated PV-battery/supercapacitor systems, and others.

Received 2nd June 2025,
Accepted 9th June 2025

DOI: 10.1039/d5tc02146d

rsc.li/materials-c

I. Introduction

The intriguing photo-physical and dielectric attributes of organic–inorganic metal halide perovskites (OIMHPs) have fascinated the scientific community. Specifically, the underlying mechanism of ion transport and relaxation dynamics is still elusive in such materials and warrants extensive investigation. Deeper insights into these mechanisms are imperative to identify the microscopic processes involved and correlate them with the performance and stability parameters of multifunctional devices based on halide perovskites, such as solar cells, high energy radiation (X-ray and γ-ray) detectors, piezoelectric nanogenerators, field effect transistors, memory devices, photo-catalysts and so on.[1–12] The OIMHPs exhibit attractive optoelectronic properties, *viz.* strong optical absorption, large photoluminescence quantum yields, low exciton binding energy, high mobility and diffusion lengths of charge carriers, *etc.*[13–15] The power conversion efficiencies (PCEs) of thin film-based solar cell devices of OIMHPs have reached up to ~25.5% in only over a decade of research.[16] However, one of the significant bottlenecks in the technological deployment of such devices is the creation of surface defects due to the prompt crystallization and grain boundary effects.[17] Several other parameters, such as ion

[a] Department of Physics, Indian Institute of Technology, Palaj, Gandhinagar 382355, India. E-mail: rupakb@iitgn.ac.in
[b] K C Patel Centre for Sustainable Development, Indian Institute of Technology Gandhinagar, Palaj, Gandhinagar 382355, India

† Electronic supplementary information (ESI) available. See DOI: https://doi.org/10.1039/d5tc02146d

migration, carrier lifetime, mobility, *etc.*, are also known to influence device performance and stability.

Single crystalline materials of these halide perovskites have been recently explored due to their significantly low trap density ($\sim 10^9$ cm^{-3}), higher diffusion length (up to ~ 1 μm), and higher carrier mobilities and the absence of grain boundaries.[18,19] Therefore, synthesizing high-quality single crystals (SCs) or highly epitaxial growth of these perovskite materials is the most feasible way forward for significant improvement in this field. However, integrating these SCs in solar cells and other energy-harvesting devices is still challenging. In the recent past, several approaches have been adopted to synthesize high-quality, large perovskite-based SCs, such as inverse temperature crystallization (ITC), anti-solvent vapor-assisted crystallization (AVC), seed crystal growth, Bridgeman method, and so on.[20–23] Among these, the ITC method is the most common for synthesizing OIMHP-based SCs because of the fast growth rate of high-quality, shape-controlled, and large-sized crystals. Saidaminov *et al.* demonstrated the rapid crystallization (within minutes) of high-quality, size- and shape-controlled $MAPbX_3$ (MA = CH_3NH_3 and X = Br or I) SCs by the ITC method.[21] Consequently, $FAPbX_3$ (FA = CH $(NH_2)_2$, X = Cl, Br, I) SCs were also studied, which demonstrated better thermal and moisture stability than the MA-based perovskite SCs.[24] FA-based, mixed halide perovskite SCs ($FAPbBr_2I$) have been used as a photodetector with stable performance. The fabricated device exhibited an excellent photo-response with a responsivity of ~ 0.8 A W^{-1} and a detectivity of $\sim 1.81 \times 10^{11}$ Jones for a visible laser ($\lambda \sim 376$ nm).[25]

A formamidinium (FA) based hybrid lead halide perovskite, like $FAPbI_3$, has an optimal band gap (~ 1.48 eV) from the perspective of perovskite-based device performance and has been the focus of the scientific community to date.[26–28] However, $FAPbI_3$ is highly unstable and cannot sustain its photoactive cubic α-phase at room temperature, degrading immediately to a photo-inactive δ-phase. This degradation is often attributed to the iodide ion migration in various literature studies.[29,30] Moreover, FA^+ also gives more thermal stability to the FA-based perovskites compared to their methylammonium (MA^+) based counterparts.[31] The halide substitution, for instance, the substitution of iodide by bromide partially, is also reported to arrest the ion migration and provide structural stability.[31,32] The replacement of iodide by bromide not only increases the bandgap, but also enhances the structural stability such that the bulk single crystalline samples could be stable in the cubic α-phase for months to even years under ambient conditions.[33,34] Hence, the mixed halide compositions of OIMHPs have proved to be vital for the application versatility.

The OIMHPs are mixed ionic–electronic conducting materials, and the understanding of ionic transport and the strength of electron–lattice interaction related to the polaronic transport, ionic polarization strength, and defect tolerance[2,35–38] is crucial for the efficient design of multifunctional energy storage and conversion devices based on such materials.[39,40] Dielectric spectroscopy is an efficient, non-destructive, and reliable technique that is widely used to probe the ionic conduction, relaxation mechanisms, polaron dynamics, *etc.*, in the OIMHPs. Several other techniques, such as blocking electrodes, Hall effect, and permeation studies, have also been employed to this end.[41]

Here, we report the synthesis of an FA-based mixed halide $FAPbBr_2I$ single crystal by the ITC method. The synthesized $FAPbBr_2I$ single crystal is characterized by X-ray diffraction (XRD), which establishes its cubic crystal structure with the $Pm\bar{3}m$ space group. The *in situ* temperature-dependent XRD, thermogravimetric analysis (TGA), and differential scanning calorimetry (DSC) demonstrate that there are no thermally induced structural changes in the $FAPbBr_2I$ SC up to 200 °C (473 K). Furthermore, the temperature-dependent (305–454 K) dielectric spectra of the $FAPbBr_2I$ sample have been investigated in a wide frequency range of 20 Hz to 10 MHz. The contribution of the resistance and capacitance of grains and the grain boundaries to the impedance is discussed quantitatively by fitting the Bode plots. The analysis of electric modulus loss spectra using the Havriliak–Negami (HN) and Kohlrausch–Williams–Watts (KWW) models and the AC conductivity spectra using the modified Jonscher's power law model at various temperatures indicates two different types of ionic conduction and hopping migration mechanisms in high-temperature (HT) and low-temperature (LT) regimes. In the LT regime (305–381 K), the DC ionic conductivity is exclusively dependent on the hopping frequency, resulting in almost similar activation energies (AEs) of ionic conduction ($E_a = 0.28 \pm 0.05$ eV) and hopping migration ($E_m = 0.29 \pm 0.05$ eV), whereas in the HT regime (395–454 K), we observed differences in both the AEs ($E_a = 0.73 \pm 0.05$ eV and $E_m = 0.49 \pm 0.05$ eV), which is attributed to the formation of mobile carriers, justified by the orders of magnitude increase in the carrier concentration factor. This difference in the AEs corresponds to the energy expended in forming these mobile carriers ($E_f = E_a - E_m = 0.24 \pm 0.05$ eV). The role of traps and the influence of mobile ions in the expected changes in the steady-state *J–V* characteristics is corroborated by the temperature-dependent space charge limited current (SCLC) measurements. The differences observed in the scaling behavior of the electric modulus and the AC conductivity spectra at different temperatures also justify the prevalence of different conduction mechanisms in both temperature regimes. These results offer vital insights into the dielectric attributes of the $FAPbBr_2I$ halide perovskite and assess its suitability for applications in optoelectronic and energy harvesting devices.

II. Experimental

A. Chemicals

Formamidinium iodide (FAI) and lead(II) bromide ($PbBr_2$) were procured from Sigma Aldrich. Gamma-butyrolactone (GBL) and *N*,*N*-dimethyl formamide (DMF) were purchased from Alfa-Aesar. All these analytical-grade reagents were used without any further purification.

B. Synthesis of $FAPbBr_2I$ single crystals

The $FAPbBr_2I$ SCs were grown using the ITC synthesis technique. 1 mmol FAI and 1 mmol $PbBr_2$ were dissolved in GBL at

60 °C. When the precursors are dissolved completely, a clear solution is formed. After that, the temperature is increased to 115 °C and kept as it is until the crystallization starts. The single crystals of $FAPbBr_2I$ then start to grow bigger within hours. The synthesis procedure and images of SCs are shown in Fig. S1(a) and (b) in the ESI.†

C. Characterization of physicochemical properties of single crystals

The powder XRD patterns of the pulverized SCs of $FAPbBr_2I$ were measured using a 9 kW Multimode XRD system (SmartLab, Rigaku Corp., Japan) for structural analysis. The X-ray source used was copper K_α (λ = 1.54 Å), and the scan rate was maintained at 1° min^{-1} with a 2θ scan range of 10° to 45°. UV-visible reflectance spectroscopy was performed using a QE-R quantum efficiency measurement system (EnliTech, Taiwan) using an integrating sphere in the reflectance measurement module. The reflectance was calibrated using a reference barium sulphite standard sample. The bandgap of the synthesized samples was deduced from the reflectance data using the Tauc plots. The thermogravimetric analysis (TGA) and differential scanning calorimetry (DSC) of the pulverized $FAPbBr_2I$ sample were performed using the PerkinElmer TG analyzer and PerkinElmer differential scanning calorimeter, respectively. The temperature-dependent space charge limited current–voltage measurements on the Ag/$FAPbBr_2I$ SC/Ag device were carried out in an in-house temperature-controlled setup using the electrical source meter provided by Keithley Instruments Inc., Model: 2601B.

D. Dielectric spectroscopy

For studying the dielectric response of the $FAPbBr_2I$ perovskite material, the electroding of the top and bottom surfaces of the $FAPbBr_2I$ pellet (pressed from the as-synthesized SCs) was done by the application of silver paste to achieve the Ag/$FAPbBr_2I$/Ag device configuration. The Keysight Impedance Analyzer E4990 was utilized to acquire the conductance and capacitance at different temperatures in the frequency range 20 Hz–10 MHz under a 0 V DC potential with a small AC perturbation potential of 0.1 V. The conductance and capacitance data were used to extract the complex impedance $Z^*(\omega)$, AC conductivity $\sigma'(\omega)$, complex dielectric constant $\varepsilon^*(\omega)$, and complex electric modulus $M^*(\omega)$. The digital image of the impedance analyzer with a PID temperature controller is also presented in Fig. S2 in the ESI.†

III. Results and discussion

Fig. 1(a) depicts the XRD profile of the $FAPbBr_2I$ single crystal perovskite at room temperature (RT) and various other temperatures up to 473 K. The XRD profiles of the $FAPbBr_2I$ single crystal show diffraction peaks at 2θ = 14.69°, 20.81°, 25.54°, 29.57°, 33.19°, 36.46° and 42.35° corresponding to the (001), (110), (111), (002), (210), (211) and (220) lattice planes, respectively. The peak profile indicates that $FAPbBr_2I$ crystallizes in a cubic crystal system with the $Pm\bar{3}m$ space group and is in agreement with previous reports on the $FAPbX_3$ (where X = Cl, Br, I, or a mixed halide) crystal structure.[25,42,43] The *in situ* temperature-dependent XRD of $FAPbBr_2I$ SC was also performed from RT to 200 °C (473 K) to examine the temperature-induced structural changes (if any) within the said temperature range. We do not observe any changes in the shape, size and number of diffraction peaks. Therefore, we conclude that there are no structural changes in the measured temperature range.

Furthermore, to probe the thermal stability of $FAPbBr_2I$ SCs, we performed the TGA and DSC measurements from RT to 473 K. The TGA and DSC plots of $FAPbBr_2I$ are shown in Fig. 1(b) and (c). The TGA trace shows no significant weight loss up to 473 K, implying that the perovskite is thermally stable in this temperature range. The DSC trace also does not show any exothermic or endothermic anomalies, confirming the thermal stability of $FAPbBr_2I$ SCs. The optical absorption of $FAPbBr_2I$ SCs is explored by UV-visible spectroscopy in the wavelength range of 300 to 1100 nm. The absorbance *versus* wavelength plot is shown in Fig. 1(d), and its inset shows the Tauc plot. The Tauc plot between $[F(R)h\upsilon]^{1/\eta}$ and $h\upsilon$ (where $F(R)$ is known as the Kubelka–Munk function, $h\upsilon$ is the energy of the incident photon, and η is a parameter determining the type of bandgap transition) is obtained from the reflectance data according to the following equation

$$F(R) = \frac{(1-R)^2}{2R}, \quad (1)$$

where R is the percentage reflectance from the sample at each wavelength. The optical band gap of ~1.97 eV is estimated from the Tauc plot considering a direct band transition, *i.e.*, η = 1/2 in the $FAPbBr_2I$ SC. The obtained bandgap value is also in agreement with previous reports.[25]

Complex impedance spectroscopy (CIS) has proven to be a remarkable technique for investigating ion dynamics and relaxation mechanisms in dielectric materials. The halide perovskites, being highly dielectric in nature, have been recently probed extensively using the CIS technique to understand the underlying phenomena behind the dynamics of ion migration, trap states, and recombination of ions inside the bulk as well as the surface of the materials.[44] Generally, the complex impedance spectra of dielectric materials can be understood by analyzing the individual contributions from grains, grain boundaries, and sample–electrode interfaces associated respectively with the high-frequency (HF), low to mid-frequency (MF), and ultra low-frequency (ULF) regions.[44,45] The temperature-dependent CIS measurements of the Ag/$FAPbBr_2I$/Ag device are manifested in the Bode plots expressed as frequency *versus* real ($Z'(\omega)$) and imaginary ($Z''(\omega)$) parts of CI. The Bode plots of $Z''(\omega)$ *vs.* ω at different temperatures (305–454 K) are shown in Fig. 2(a)–(d), and the equivalent circuit model to fit the data is shown in the insets. In our measurement configuration of the Ag/perovskite/Ag device, we have the perovskite in the polycrystalline pellet form composed of grains and grain boundaries (GBs). Hence, we can represent this system by a Maxwell–Wagner equivalent electrical circuit having two parallel RC circuits connected in series, each corresponding to a physical

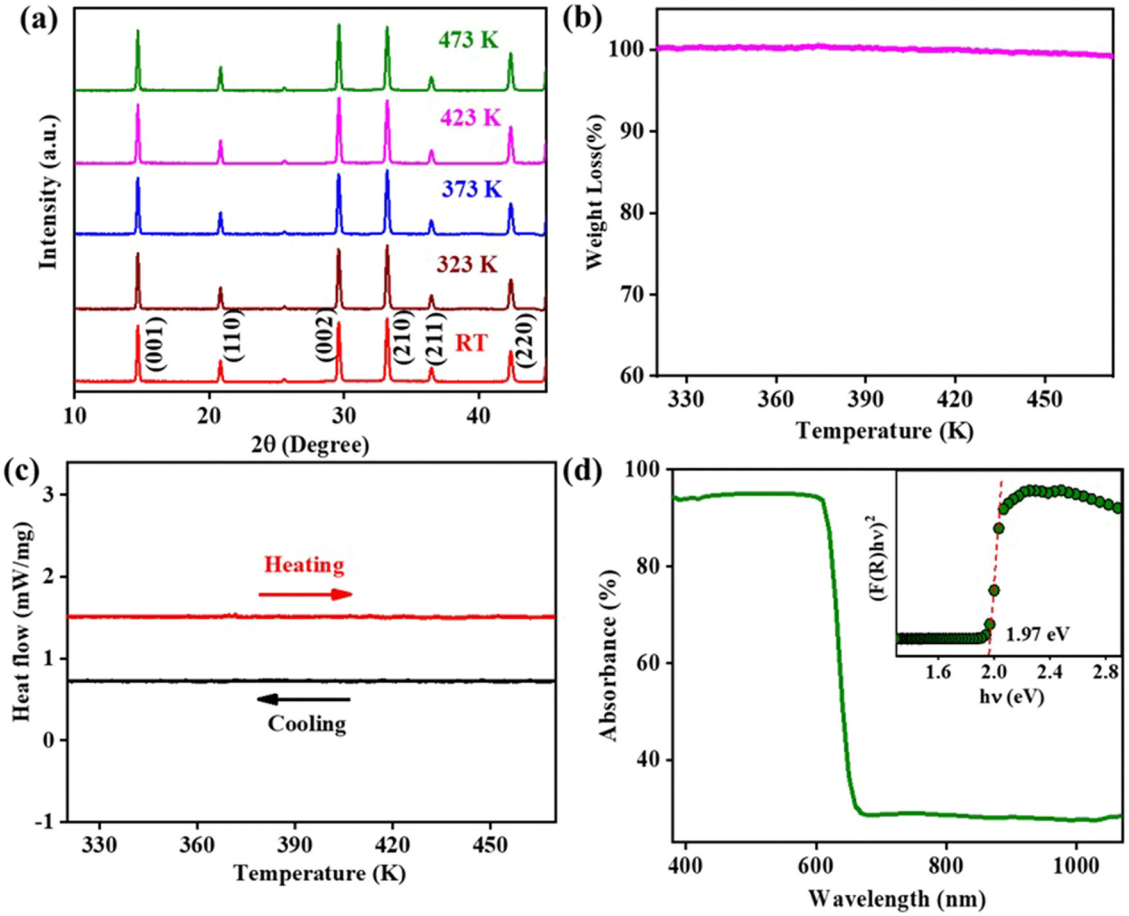

Fig. 1 (a) *In situ* temperature-dependent XRD profiles of pulverized $FAPbBr_2I$ SCs at different temperatures, (b) the TGA trace, (c) the DSC heating and cooling traces in the temperature range of RT to 473 K, and (d) the UV-vis absorption profile of $FAPbBr_2I$ SCs with the inset showing the Tauc plot for energy bandgap calculation.

process happening in the grain and GBs. The real ($Z'(\omega)$) and imaginary ($Z''(\omega)$) parts of impedance for such a model are given by:[46]

$$Z'(\omega) = \frac{R_1}{1+\omega^2 R_1^2 C_1^2} + \frac{R_2}{1+\omega^2 R_2^2 C_2^2} \quad (2)$$

$$Z''(\omega) = -\left(\frac{R_1^2 \omega C_1}{1+\omega^2 R_1^2 C_1^2} + \frac{R_2^2 \omega C_2}{1+\omega^2 R_2^2 C_2^2}\right) \quad (3)$$

where both the RC elements will exhibit the respective time constants:

$$\tau_1 = \frac{1}{\omega_1} = R_1 C_1 \quad (4)$$

$$\tau_2 = \frac{1}{\omega_2} = R_2 C_2 \quad (5)$$

where R_1 and C_1 are the resistance and capacitance of grains and R_2 and C_2 are the resistance and capacitance of GBs. It is known that a parallel RC circuit represents a relaxation process, and we associate these with space charge relaxations in grains and GBs. Furthermore, it is also established that the space charge relaxation, *i.e.*, the reorganization of space charges, happens slowly in the GBs (or at any interface for that matter) compared to the grains because GBs are the area of discontinuous electrical changes while grains have a continuous isotropic electrical environment, which facilitates faster reorganization of charges. Hence, the dynamics at GBs will correspond to the relaxation at lower frequencies (slower reorganization) and the dynamics at grains will correspond to the relaxation at slightly higher frequencies (comparatively faster reorganization than that happening at the GBs). The frequency dependence of $Z''(\omega)$ for the $Ag/FAPbBr_2I/Ag$ device at different temperatures demonstrates broad relaxation peaks. This broadening observed in the relaxation peaks is due to the distribution of relaxation times and suggests a non-Debye relaxation behavior in $FAPbBr_2I$.[47,48]

Fig. S3(a–j) (ESI†) also presents the fitted Bode plots of the real part of CI: $Z'(\omega)$ *vs.* ω at various temperatures. The values of $Z'(\omega)$ decrease with increasing temperature, indicating that $FAPbBr_2I$ follows a negative temperature coefficient of resistance, typical of semiconductors. At low frequencies ($\omega \to 0$), the impedance is very high ($Z'(\omega) \to (R_1 + R_2)$, according to eqn (2)), and at high frequencies ($\omega \to \infty$), the circuit offers very low impedance ($Z'(\omega) \to 0$). Physically, inside our system, at LFs, the free ions are able to follow the applied AC field and move inside the system from grains towards GBs; hence, they

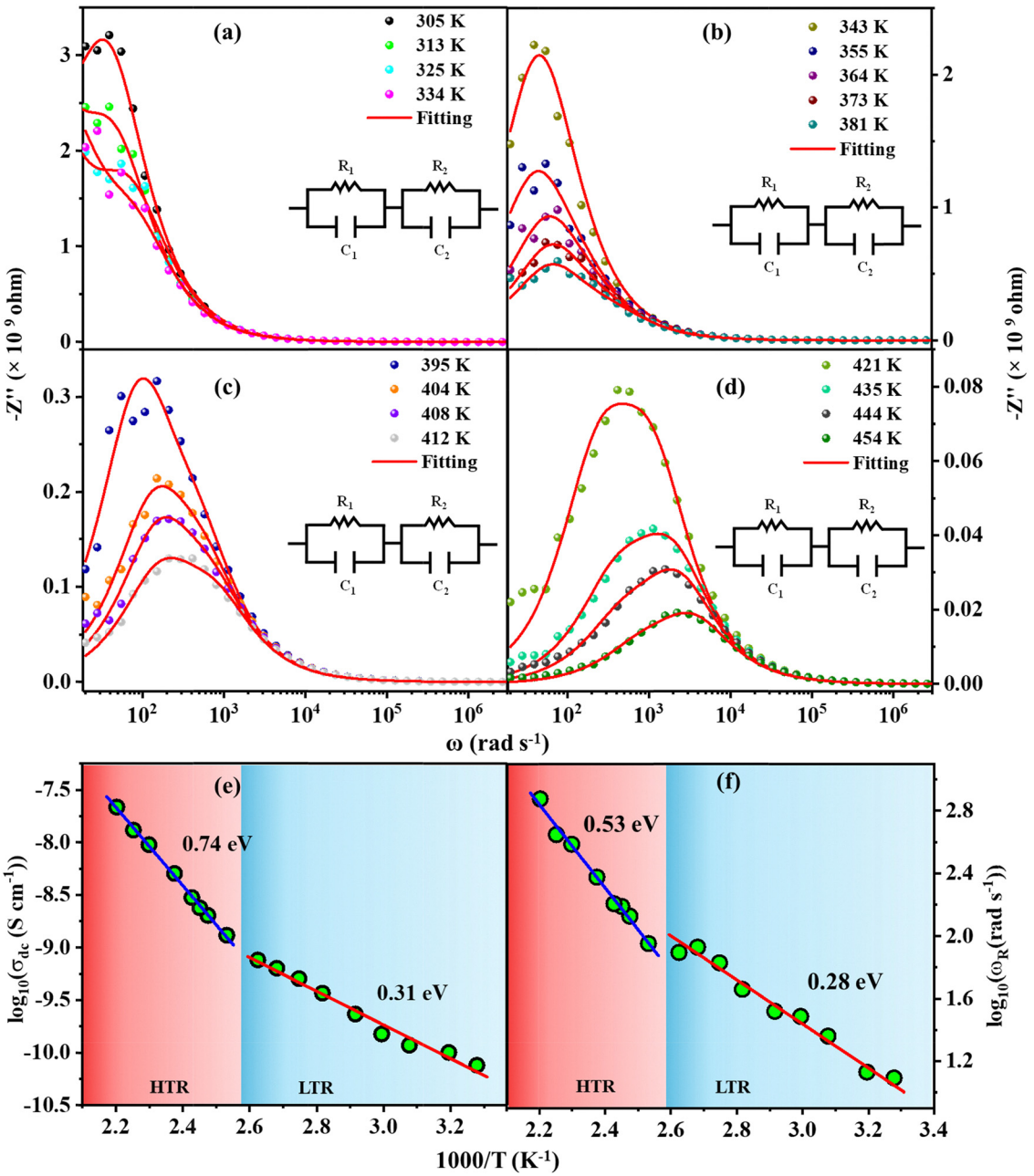

Fig. 2 Bode plots of the imaginary part of impedance fitted by a Maxwell–Wagner equivalent circuit at different temperatures: (a) 305–334 K, (b) 343–381 K, (c) 395–412 K, and (d) 421–454 K. Insets depict the equivalent circuit model. Arrhenius plots of (e) DC ionic conductivity and (f) hopping frequencies of space charge relaxation obtained from impedance data.

experience a very high impedance contribution from both grains and GBs. Usually, at LFs, the resistors act as the short circuit path, and capacitors block DC; hence, the effective impedance is primarily the resistive contribution of grains and GBs. While at high frequencies, we know that resistances block AC field and capacitors act as short circuits and pass the AC signal; hence, the impedance falls significantly at higher frequencies with an inverse dependence on the frequency of the AC field ($Z'(\omega) \sim 1/\omega$). This transition from high to low impedance should occur at the effective relaxation frequency (ω_R) of the equivalent circuit. With the increment in temperature, this transition occurs at larger effective relaxation frequency, which is natural because the ionic movement is temperature activated and long-range motion persists more at higher temperatures.

The values of these parameters (R_1, C_1, and R_2, C_2) obtained by fitting the Bode plots of $Z''(\omega)$ and $Z'(\omega)$ at all the measurement temperatures are presented in Table S1 in the ESI.† The resistance of GBs and grains and their difference ($R_2 - R_1$) is observed to decrease with the increment in temperature (Fig. S3(k) in the ESI†). The variation of grain and GB-capacitance with temperature is also shown in Fig. S3(l) in the ESI.†

We have calculated the DC conductivity (σ_{dc}) at different temperatures from the impedance data by using the relation: $\sigma_{dc} = \frac{t}{RA}$, where t is the thickness, A is the area of the sample, and R is the total resistance offered by the sample. Here, the total resistance is a sum of grain and grain-boundary resistance, *i.e.*, $R = R_1 + R_2$, t = 0.8 mm, and A = 8 mm^2. The σ_{dc} obtained from impedance data as a function of 1000/T follows the Arrhenius relation shown in Fig. 2(e), and we observe two different activation energies (AEs) of ion conduction (E_a) obtained from the Arrhenius plots in two different temperature regions, which we designate as the low and high-temperature regions (LTR and HTR). The obtained values of activation energies in the LTR and HTR are 0.31 ± 0.05 eV and 0.74 ± 0.05 eV. Furthermore, we also calculated the effective relaxation frequencies (ω_R) at all the measured temperatures from the impedance data. The expression of ω_R is derived in the Note S1 (ESI†). Typically, ω_R is the frequency value at which the imaginary impedance ($Z''(\omega)$; representing relaxation) becomes maximum. The simplified expression of effective relaxation frequency is $\omega_R = \omega_1\omega_2/\sqrt{(\omega_1^2 + \omega_2^2)}$, where ω_1 and ω_2 are the relaxation frequencies corresponding to the grains ($1/R_1C_1$) and GBs ($1/R_2C_2$) using eqn (4) and (5). It is noteworthy that the term "effective relaxation frequency" should not be taken analogous to the single RC component, nor it is intended to imply a single relaxation mechanism. It arises from a combination of grain and GB relaxations and is used solely for plotting an Arrhenius relation to estimate activation energy. The plot of log(ω_R) *vs.* 1000/T also follows the Arrhenius behavior since hopping is a temperature-activated phenomenon. The AEs of hopping migration (E_m) in the LTR and HTR were estimated as 0.28 ± 0.05 eV and 0.53 ± 0.05 eV, respectively. The plausible reasons and the implications of observing two different AEs in LTR and HTR as well as differences in E_a and E_m in the HTR are discussed later in the AC conductivity section.

The coupled ionic–electronic behavior forms a complex problem in the halide perovskite materials because of the multiple physical processes manifesting in different types of dielectric polarization.[2,49] While the impedance spectra help us understand how the system impedes the charge transport, the permittivity spectra shed light on the different polarization contributions in the system. The various physical processes include electronic, ionic, dipolar or orientational, and space charge (resulting from redistribution of free ions and electrons) polarizations, which contribute to the relative permittivity. All these components, due to the respective physical processes, occur at a diverse range of time scales ranging from femtoseconds to seconds. The real and imaginary parts of the frequency-dependent complex dielectric constant can be expressed as:

$$\varepsilon'(\omega) = -\frac{Z''}{\omega C_0(Z'^2 + Z''^2)} \quad (6)$$

$$\varepsilon''(\omega) = \frac{Z'}{\omega C_0(Z'^2 + Z''^2)} \quad (7)$$

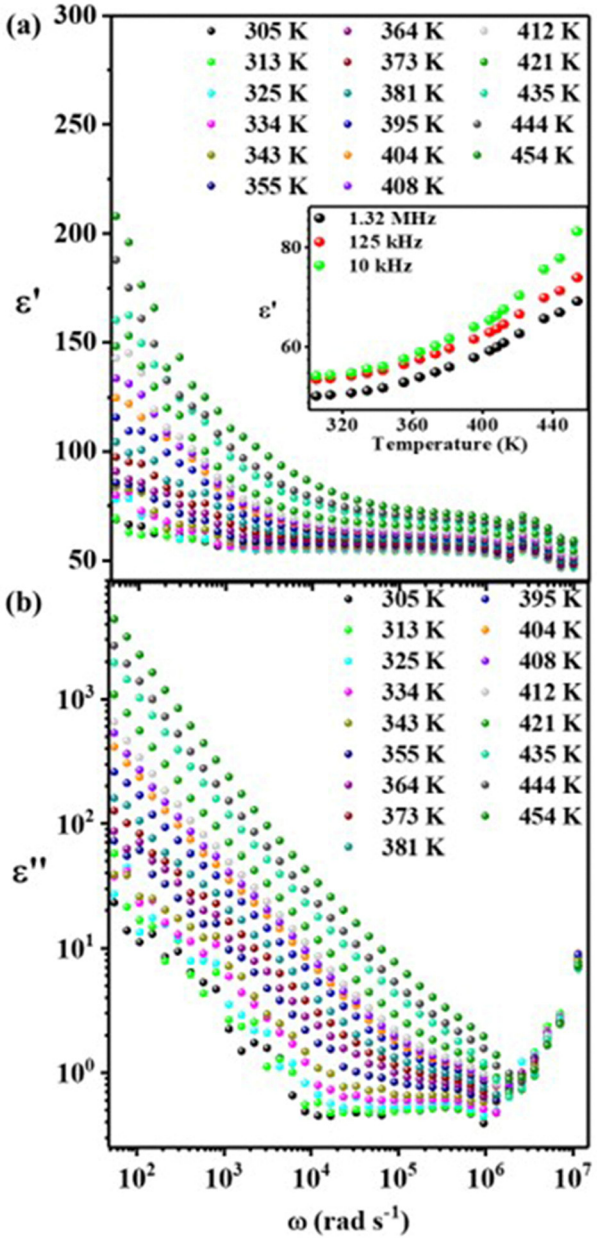

Fig. 3 Temperature-dependent (305–454 K) dielectric (a) relative permittivity and (b) loss spectra of the $FAPbBr_2I$ perovskite.

The real part of the dielectric constant (ε') *vs.* ω for the $FAPbBr_2I$ perovskite is plotted at various temperatures (305–454 K), shown in Fig. 3(a). The value of the dielectric constant is higher at LFs, as expected, due to the Maxwell–Wagner space charge effects.[2] The ionic movement is a slow process, and at lower frequencies, the slow switching of the AC field does not affect the long-range ionic movements, and thus the ions move across long distances. Hence, they accumulate at the GB interfaces and contribute to the space charge polarization. That is why we observe high relative permittivity values at LFs, which fall off as the frequency is increased because long-range ionic

motion is less significant as the frequency is increased. Typically, after the resonant frequency (corresponding to the relaxation of space charges), other contributions, *viz.* dipolar, atomic, and electronic polarizations, take over. Hence, physically, in our system, the ionic movement (at LFs) from grain towards GBs experiences the impedance from both grains and GBs and forms a space-charge layer at GB interfaces, which primarily contributes to the space charge polarization and hence the dielectric permittivity. Furthermore, the dielectric permittivity is observed to increase at LFs as we increase the temperature, further confirming the Maxwell–Wagner space charge polarization effect, which corresponds to the temperature activated ionic conduction and hopping transport.

The room temperature (RT) value of ε' for $FAPbBr_2I$ varies from 52 to 56 in the kHz to MHz frequency range and agrees with the reported values on various $FAPbX_3$ perovskites.[50] The temperature variation of ε' in the HFs (1 kHz to 1.32 MHz) is also presented in the inset of Fig. 3(a). The ε'–T curve at HFs also shows temperature dependence (weaker dependence as compared to that at the LFs) and can be attributed to the dipolar relaxation of the reorienting FA^+ dipoles. S. Govinda *et al.*[51] also reported strong evidence of the MA^+ dipole orientation in the tetragonal phase of $MAPbX_3$ by observing a strong temperature dependence of ε' compared to temperature-independent ε' in $CsPbBr_3$ at the kilohertz to megahertz frequencies. They also quantified the large contribution of MA^+ dipoles and almost a negligible effect of Maxwell–Wagner space-charge polarization in this frequency range. Therefore, the temperature-dependency of ε' (inset of Fig. 3(a)) in the case of the $FAPbBr_2I$ perovskite clearly suggests the role of FA^+ dipolar contribution. Notably, the ε'–T dependency in our case is also observed to change with frequency but is not as strong as in the reported $MAPbX_3$ perovskites, which were measured at temperatures lower than RT. Our range of temperatures are much higher (305–454 K), which induces extrinsic effects other than mere dipolar contributions.[51] Additionally, $FAPbBr_2I$ exhibits the cubic phase, and FA^+ possesses a lower dipole moment compared to MA^+.[52] The nature of the frequency-dependent dielectric loss $\varepsilon''(\omega)$ spectra is shown in Fig. 3(b). The dielectric loss spectra are defined as[17,53]

$$\varepsilon''(\omega) = \frac{\sigma'(\omega)}{2\pi\varepsilon_0\omega} \tag{8}$$

In accordance with the Jonscher power law (JPL), identified by $\sigma' = \sigma_{dc} + A\omega^s$ (σ_{dc} is the DC ionic-conductivity, A is a prefactor, and s is an exponent; $0 < s < 1$),[54] the expression (8) becomes:

$$\varepsilon''(\omega) = \frac{\sigma_{dc}}{2\pi\varepsilon_0\omega} + \frac{A}{2\pi\varepsilon_0\omega^{1-s}} \tag{9}$$

The $\varepsilon''(\omega)$ varies as $\sim\frac{1}{\omega}$ in the LFs corresponding to the DC ionic conductivity and as $\sim\frac{1}{\omega^{1-s}}$ in the dispersive or JPL region. In the LFs, we observed the DC region $\left(\sim\frac{1}{\omega}\right)$ at all temperatures, implying the long-range ionic conductivity of space charges. However, the dispersive region (kilohertz to megahertz) exhibits nearly constant loss (NCL) in the LTR (regions with almost constant ε''), corresponding to $s \approx 1$, and decreasing loss in the HTR (ε'' decreases faster with ω as temperature increases), corresponding to a strongly decaying s with temperature. The s-values at different temperatures are also quantified in the analysis of the AC conductivity in a later section. The dielectric loss in a material decreases with an increment in the frequency of the applied AC field, because the contribution of space charge and dipolar polarization decreases significantly.[55] In our observation of loss spectra of $FAPbBr_2I$, in the LT and dispersive region (kHz–MHz), where we can find a region with $s \approx 1$, the FA^+-dipoles are able to reorient and dipolar polarization is still stronger to contribute to the NCL, whereas the Maxwell–Wagner polarization (MWP) will not be significant because the space charges will not have enough time to accumulate at the interfaces. In the HT and dispersive regions, where s decreases strongly with temperature, the contributions from both MWP and FA^+-dipolar reorientation will be more insignificant and hence implies the faster decay of loss spectra as we increase the temperature.

The AC conductivity spectra of the Ag/$FAPbBr_2I$/Ag device are also studied in detail to gain critical insights into the mechanisms behind thermally activated ionic conduction and hopping migration. The conductivity spectra $\sigma'(\omega)$ of $FAPbBr_2I$ at various temperatures (305–454 K) and the corresponding fits using the Almond–West model (a modified form of JPL) in terms of DC conductivity (σ_{dc}), hopping frequency (ω_H) and power law exponent (s) with a limiting value of $0 \leq s \leq 1$ are displayed in Fig. 4(a) and are given as[54,56]

$$\sigma'(\omega) = \sigma_{dc}\left[1 + \left(\frac{\omega}{\omega_H}\right)^s\right] \tag{10}$$

The fitting parameters (σ_{dc}, ω_H and s) at different temperatures are compiled in Table SII in the ESI.† Generally, in a dielectric material, the LF region is dominated by the long-range transport of ions,[37,45,57] which results in the successful hopping of these ions from one lattice site to another.[58] We, therefore, observe a frequency-independent DC conductivity (σ_{dc}) in the LF region. The DC conductivity region then crosses over (at $\omega = \omega_H$) to a frequency-dependent dispersive region at the HF region. The dispersive nature of conductivity at high frequencies can be explained by the time-evolution of correlated forward–backward hopping of ions, as formulated in Funke's Jump-Relaxation Model.[58]

The ionic conduction and hopping migration follow the Arrhenius law because they are thermally activated processes:

$$\sigma_{dc} = \sigma_0 \exp\left(-\frac{E_a}{k_B T}\right) \tag{11}$$

$$\omega_H = \omega_0 \exp\left(-\frac{E_m}{k_B T}\right) \tag{12}$$

where σ_0 and ω_0 are the Arrhenius prefactors and E_a and E_m are the AEs of ionic conduction and hopping migration. The

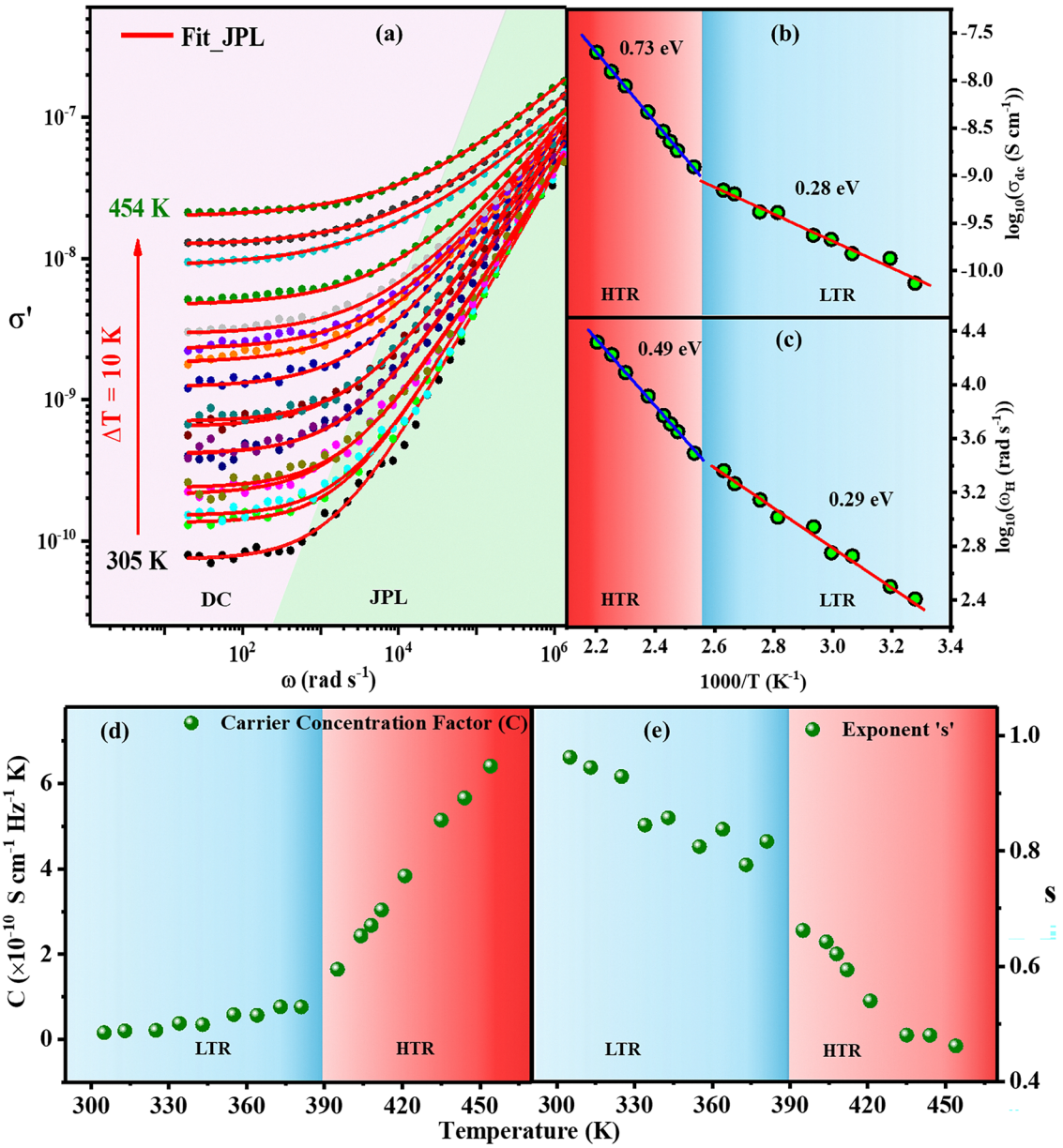

Fig. 4 (a) Temperature-dependent (305–454 K) AC conductivity spectra fitted by the modified Jonscher power-law, Arrhenius plots of (b) DC-conductivity and (c) hopping frequency obtained from power-law fits of AC conductivity, temperature dependence of (d) the ionic carrier concentration factor, and (e) power-law exponent of the $FAPbBr_2I$ perovskite.

obtained value of $\log(\sigma_{dc})$ from power law fits is plotted with $1000/T$ and is shown in Fig. 4(b). The Arrhenius plot exhibits two distinct regions of temperature, *viz.* the low-temperature region (LTR) from 305 K to 381 K and the high-temperature region (HTR) from 395 K to 454 K. The estimated values of AEs and E_a from the slopes of Arrhenius plot in the LTR and HTR are 0.28 ± 0.05 eV and 0.73 ± 0.05 eV, respectively. We also plotted $\log(\omega_H)$ *vs.* $1000/T$ as shown in Fig. 4(c) and obtained the AE of hopping migration E_m in the LTR and HTR respectively to be 0.29 ± 0.05 eV and 0.49 ± 0.05 eV. We observed that the AEs of ionic conduction and hopping migration have similar values ($E_a \approx E_m$) in the LTR, whereas the differences in the AEs ($E_a - E_m \approx 0.24 \pm 0.05$ eV) in the HTR indicate a temperature-triggered interplay of ionic conduction and hopping migration.

The general expression of the DC ionic conductivity of any given material is given as:[59]

$$\sigma_{dc} = c\left(\frac{z^2F^2}{k_BT}\right)\eta\alpha_0^2\omega_H \quad (13)$$

where c is the concentration of mobile ions, z is the charge of each ion, F is the Faraday constant, k_B is the Boltzmann constant, η is the geometric factor, and α_0 is the hopping

distance.[60] We introduce a new constant C, which represents the relative carrier concentration of ions and is given as:

$$C = c\left(\frac{z^2F^2}{k_B}\right)\eta\alpha_0{}^2 \quad (14)$$

Therefore, the expression for DC conductivity becomes:

$$\sigma_{dc}T = C\omega_H \quad (15)$$

Generally, if the mobile carriers are not thermally activated, the carrier concentration factor C is independent of temperature, and the temperature response of ionic conductivity is only dependent on hopping frequency ($E_a = E_m$)[59] and they follow a common conduction and relaxation mechanism. However, when the mobile carriers are thermally activated, the factor C itself is temperature-dependent and follows an Arrhenius relationship:

$$C = C_0\exp\left(-\frac{E_f}{k_BT}\right) \quad (16)$$

where the prefactor C_0 is the effective carrier concentration and E_f is the AE for the formation of free carriers. Therefore, in light of eqn (16), the Arrhenius relation of σ_{dc} becomes:

$$\sigma_{dc} = \sigma_0\exp\left(-\frac{(E_m + E_f)}{k_BT}\right) \quad (17)$$

and therefore, the AE of ionic conduction in the case of thermally activated carrier formation has two components:

$$E_a = E_m + E_f \quad (18)$$

In the case of $FAPbBr_2I$, we calculated the values of the carrier concentration factor C at all temperatures using eqn (15) and fitted parameters (σ_{dc}, ω_H). The C *vs.* T plot in the temperature range (305–454 K) is presented in Fig. 4(d). From the C–T plot, we clearly observe that C is almost constant in the LTR (305–381 K), justifying the similar values of AEs ($E_a \approx E_m$) obtained in this temperature regime. However, C increases by orders of magnitude in the HTR (395–454 K) and confirms the thermally activated mechanism where the concentration of mobile ions has increased substantially by overcoming the barrier E_f($E_a - E_m \approx 0.24 + 0.05$ eV) and is responsible for the difference in the observed AEs.

We propose a plausible mechanism in which the traps play a crucial role in the thermally activated ionic conduction and hopping process. The traps formed in the MHPs are attributable to the presence of vacancies, interstitial, anti-site substitution defects, *etc.*[61] The additional mobile ions might be generated *via* defect dissociation, ionization of neutral species, or any other relevant process. In other words, these ions were earlier trapped in the LTR because of insufficient thermal energy to overcome the potential well, whereas in the HTR, the thermal energy is sufficient to dissociate and make them free.[59,62] The substantial increase in the ionic carrier concentration factor C with temperature (Fig. 4(d)) also indicates the crucial role of traps in ionic conduction. The barrier E_f for overcoming the formation of mobile ions corresponds here to the trap potential. Hence, the increase of ionic concentration leads to different activation barriers (E_a and E_m) in the HTR (395–454 K).

Additionally, another pertinent question arises as to why E_m itself would increase from 0.28 eV (in the LTR) to 0.49 eV (in the HTR). This can be addressed as follows: since the ion concentration is temperature-independent in the LTR, it suggests that the system has a constant defect population (*e.g.*, intrinsic vacancies), which is synthetically created and cannot be avoided. This would predominantly lead to independent hopping of ions. However, when the ion concentration is temperature-dependent (as observed in the HTR), it suggests thermal generation of additional mobile ions. This would lead to increased ion–ion interactions and possibly enhanced correlated ionic hopping (rather than independent hopping across barriers), thus increasing the activation barrier. This idea is also supported by the observed temperature-dependent changes in the frequency exponent (s) as depicted in Fig. 4(e). In the LTR (305–381 K), the exponent (s) varies slightly from 0.96 (at 305 K) to 0.81 (at 381 K) and is close to 1, which indicates a nearly constant loss (NCL) or the hopping of each ion is independent of each other between localized sites,[63] whereas in the HTR (395–454 K), s decreases significantly to lower values from 0.66 (at 395 K) to 0.46 (at 454 K) and a sudden jump from 0.81 (at 381 K) to 0.66 (at 395 K) is observed. This indicates that the ion hopping is no longer independent; rather, it is a correlated hopping of ions between localized sites[64] due to enhanced ion–ion interactions *via* generation of additional free ions. This correlated ion transport would, more often than not, increase the energy barrier for hopping. Hence, the variation of s with temperature clearly indicates a sudden change of AEs in two different temperature regimes and direct implications can be made to correlate different kinds of ionic transport in different regions of temperature. For the broader context, we have also compared the activation energies associated with the hopping migration of various species (ions/vacancies) in the OIMHPs, estimated *via* a wide variety of experimental techniques (see Table 1).

To gain further insights into the role of trap states and trapped carriers in understanding the thermally activated ion conduction and hopping in $FAPbBr_2I$ perovskites, we have investigated the temperature-dependent space charge limited current–voltage characteristics. We have discussed the effect of mobile carrier formation at HT on influencing the corresponding steady-state SCLC characteristics. The presence of localized states in the sub-bandgap region, known as traps, is commonly observed due to the high degree of energetic and spatial disorders in the MHPs.[61,73] Due to the presence of these trap-states, there is accumulation (or trapping) of charge species, and the current due to the free carriers is limited by these space charges. Usually, in a trap-free device, there are two regions, namely an ohmic region (J–V) at very low voltages dominated by background carrier density,[74,75] followed by the space charge limited current (SCLC) region ($J \sim V^2$) after crossing a certain threshold voltage. The SCLC region occurs due to increased carrier density (due to the injection of charges after crossing the threshold voltage) compared to the background carrier density. The SCLC follows the Mott–Gurney Law:[76]

$$J = \frac{9}{8}\varepsilon_0\varepsilon_r\mu\frac{V^2}{L^2} \quad (19)$$

Table 1 Comparison of the activation energies associated with the hopping migration in the OIMHPs, estimated using a wide variety of experimental techniques

S. No.	Material composition	Migrating species	Activation energy (eV)	Technique	Ref.
1	$MAPbI_3$	I^-	0.17	Nuclear quadrupole resonance (NQR)	65
2	$MAPbI_3$	I^-	0.29 ± 0.06	Transient ion drift	66
3	$MASnI_3$	Iodide vacancy (V_I) Iodide interstitial (I_i)	0.37 0.65	Density functional theory (DFT)	67
4	$MASnBr_3$	Br^-	0.44	Solid-state nuclear magnetic resonance (NMR)	68
5	$MAPbI_{3-x}Cl_x$	I^-	0.55	Impedance and intensity modulated photovoltage spectroscopy (IMVS)	69
6	$FAPbI_3$	I^-	0.222 ± 0.015	Temperature-dependent J–V	70
7	$MA_{0.5}FA_{0.5}PbI_3$	I^-	0.296 ± 0.015	Temperature-dependent J–V	70
8	$FAPbBr_{2.9}Cl_{0.1}$	Br^-	0.58	Temperature-dependent J–V	71
9	$FAPbBr_3$	Bromide vacancy (V_{Br}) Bromide interstitial (I_{Br}) FA vacancy (V_{FA}) FA interstitial (I_{FA})	0.33 0.24 0.39 0.34	Density functional theory (DFT)	72
10	$FAPbBr_2I$	Halide (Br/I) Not conclusive which halide	0.30 ± 0.05 (low temperature (305–381 K)) 0.50 ± 0.05 (high temperature (395–454 K))	Temperature-dependent impedance spectroscopy	This work

where ε_0, ε_r, and μ are the permittivity of free space, the dielectric constant of the material and charge carrier mobility, respectively. J, V, and L are the current density, applied voltage, and thickness of the device. Now, if we introduce the traps and consider the trapped charge carrier density in the current density calculations from Poisson's equation,[75,77] a third region due to the filling of trap states, commonly known as the trap-filled limited (TFL) region, is also introduced in between the ohmic and SCLC regions. The current density in the TFL region is sharply increased ($J \sim V^{\beta}$, with $\beta > 2$) after crossing an onset voltage (V_{ons}),[78] expressed as:

$$V_{ons} \approx \frac{en_t L^2}{2\varepsilon_0 \varepsilon_r} \quad (20)$$

where n_t is the density of trapped carriers.

The experimentally determined log–log plots of J–V characteristics for the Ag/$FAPbBr_2I$ SC/Ag device configuration at different temperatures such as 100 °C (373 K), 120 °C (393 K), 140 °C (413 K) and 160 °C (433 K) are presented in Fig. 5. The digital images of the lateral device architecture of the Ag/$FAPbBr_2I$ SC/Ag device are presented in Fig. S4(a and b) in the ESI.† In the log–log plot, all the regions, *viz.* ohmic, TFL, and SCLC, are fitted separately in accordance with the generic scaling law of J–V, *i.e.*, $J \sim V^{\beta}$ in the respective regions. Several reports[75,79,80] have demonstrated by the drift-diffusion (DD) simulation studies that mobile ions can strongly influence the typical SCLC characteristics because they can screen/negate the charge of trapped carriers (e^- or h^+). Hence the density of trapped carriers expressed by eqn (20) can be underestimated by orders of magnitude depending on the difference between mobile ion density and trapped carrier density. Duijnstee *et al.*[75] showed that if the mobile ions are introduced then V_{ons} shifts to lower values and when the value of ion density outnumbers the trapped carrier density, then the effect of traps is eventually overshadowed and we cannot observe the TFL region. In effect, if traps dominate, then the TFL region can be observed and if mobile ion density dominates the traps, then the TFL region could no longer be observed.

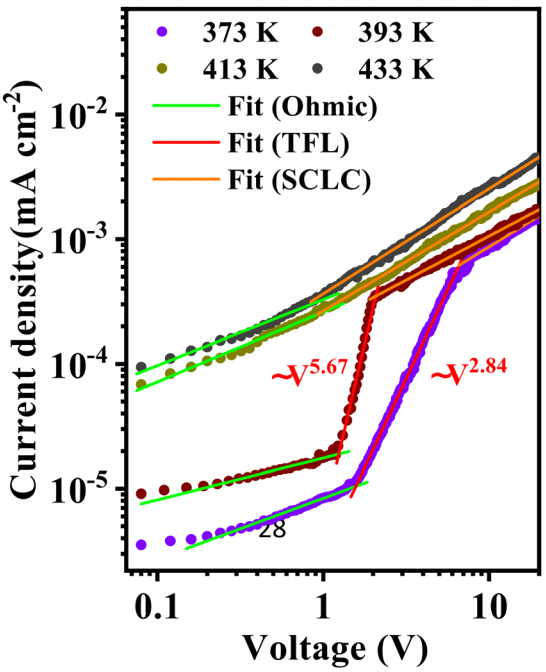

Fig. 5 Temperature-dependent space charge limited current–voltage (J–V) characteristics of the Ag/$FAPbBr_2I$ SC/Ag device configuration at temperature T = 373 K, 393 K, 413 K, and 433 K.

Remarkably, from our observations of the ionic carrier concentration factor *vs.* temperature in the conductivity section, the value of C has increased significantly in the HTR (Fig. 4(d)). Moreover, this increase is also justified by the observance of an AE barrier of forming these carriers, as indicated in the Arrhenius plots of DC conductivity and hopping frequency (Fig. 4(b) and (c)). The onset voltage (V_{ons}) is determined from the crossover point of the ohmic to the TFL

region. The values of V_{ons} at 100 °C (373 K) and 120 °C (393 K) from the *J–V* plots are found to be 1.57 V and 1.24 V, respectively. Notably, we cannot use V_{ons} in eqn (20) for extracting trap density because the ion migration would lead to the hysteresis effect[80,81] and this value of V_{ons} would be different for forward and reverse scans. In this context, researchers have also introduced the pulsed-voltage SCLC technique for halide perovskites[75,79,80] where one can measure the hysteresis-free *J–V* characteristics and extract these device parameters more reliably. Therefore, we only consider the forward scan *J–V* characteristics at all temperatures for extracting V_{ons} for a qualitative comparison. In addition, our primary focus is on observing the changes in the nature of *J–V* characteristics from the LTR to the HTR, which would help us to interpret the effect of mobile ion dynamics on the nature of steady state *J–V* characteristics.

The values of V_{ons} decrease as expected because the ion density increases with temperature, negating the charge of trapped carriers. Eventually, the ion density might have outnumbered the traps beyond a critical temperature of 395 K and hence we conclude that the large number of mobile carriers formed in the HTR by the temperature triggered mechanism is responsible for the absence of the TFL region at 413 K and 433 K. The slope of the TFL regime was also observed to increase from ~2.84 at 373 K to ~5.67 at 393 K. In this way, we have demonstrated that the effect of transient ionic mechanisms, *viz.* thermally activated formation of mobile ions and differences in the AEs of ionic conduction and hopping migration, is very well manifested in the nature of steady-state SCL *J–V* characteristics. In addition to the observation of the influence of mobile ions on the expected changes of the nature of *J–V* characteristics, the observed changes in the *J–V* characteristics also corroborate the role of traps in understanding the thermally activated interplay of ionic conduction and hopping migration in the mixed halide $FAPbBr_2I$ perovskite.

In order to investigate the relaxation mechanisms involved in the $FAPbBr_2I$ perovskites, the electric modulus loss spectra $M''(\omega)$ are investigated in the temperature range of 305 K to 454 K. The electric modulus is expressed as the reciprocal of complex dielectric permittivity $M^*(\omega) = 1/\varepsilon^*(\omega)$. The CEMS serves as a powerful tool to analyze relaxation phenomena, specifically in materials where electrode polarization or large DC conductivity may obscure bulk features in the permittivity or impedance spectra.[82] As evident from the mathematical expression or formalism of electric modulus (reciprocal of complex permittivity), it suppresses the effects of large capacitance contributions (such as from interfacial regions of grain boundaries or electrodes) and emphasizes the bulk relaxation dynamics of charge carriers.[82,83] In contrast to the impedance formalism, which highlights regions of high resistance (like grain boundaries), the modulus spectrum is more sensitive to regions of low capacitance, such as the grains or bulk.

The frequency dependence of $M''(\omega)$ at different temperatures, presented in Fig. 6(a), shows distinctive relaxation peaks and is ascribed to the relaxation of space charges at the characteristic frequency of the material. These peaks are also indicative of the transition from long-range ionic motion at the LF region to localized, short-range motion at the HF region. The $M''(\omega)$ peaks also shift towards the HF side, suggesting the thermally activated relaxation process. The $M''(\omega)$ spectra of the $FAPbBr_2I$ perovskite show asymmetric relaxation peaks characteristic of the non-Debye type of relaxation.[47] The imaginary part of the Havriliak–Nigami (HN) model is used to fit the asymmetric curves of $M''(\omega)$ spectra observed for $FAPbBr_2I$:[84]

$$M^*(\omega) = M_\infty + \frac{M_s - M_\infty}{[1 + (j\omega\tau_{HN})^{\alpha_{HN}}]^{\gamma_{HN}}} \quad (21)$$

where M_s and M_∞ are the limiting values respectively at LF and HF and τ_{HN} is the relaxation time in the HN model. The HN shape parameters are defined by α_{HN} and γ_{HN}, with $0 < (\alpha_{HN}$ or $\gamma_{HN}) \leq 1$ as the limiting conditions.[85] The fitted plots of $M''(\omega)$ spectra, using the imaginary part of eqn (21), at different temperatures are shown in Fig. 6(a), and the parameters obtained from the best fits are listed in Table SIII in the ESI.† The relaxation time τ_{HN} calculated using the HN model for both the LTR and the HTR obeys the Arrhenius equation,

$$\tau = \tau_0 \exp\left(\frac{E_{HN}}{k_B T}\right) \quad (22)$$

The plot of $\log_{10}\tau$ *vs.* reciprocal temperature is shown in Fig. 6(b), and the activation energies obtained in the LTR and HTR are E_{HN1} = 0.29 ± 0.05 eV and E_{HN2} = 0.49 ± 0.05 eV respectively. These values are coherent with the AEs of hopping migration in the LTR and HTR, obtained from the Arrhenius plots of hopping frequency, validating different hopping mechanisms in LTR and HTR regions. The shape parameters are also plotted as a function of temperature in Fig. 6(c) and observed to follow complementary variations with temperature.

The experimentally observed relaxation behavior in the $FAPbBr_2I$ perovskite is also analyzed by the well-known time domain relaxation model, Kohlrausch–Williams–Watts (KWW) function, given by[86,87]

$$\phi(t) \approx \exp\left(-\left(\frac{t}{\tau_{KWW}}\right)^{\beta_{KWW}}\right) \quad (23)$$

The KWW function, $\phi(t)$, represents the decay of the applied electric field $E(t)$ inside the material. The τ_{KWW} is the KWW relaxation time, and β_{KWW} ($0 \leq \beta_{KWW} \leq 1$) is the stretched exponent, typically used for the materials obeying slow relaxation dynamics.[88] β_{KWW} is a very useful parameter that distinguishes the Debye- and non-Debye-types of relaxation of mobile ions. The Debye-type relaxation is indicated when β_{KWW} obtains or tends to the value of 1. The values $0 < \beta_{KWW} < 1$ suggest the non-Debye relaxation, and β_{KWW} = 0 for maximum dipole–dipole interaction.[89] The values of β_{KWW} for the $FAPbBr_2I$ perovskite were observed to vary from ~0.61 at 305 K to ~0.58 at 454 K with random increment or decrement in between the temperature range without any specific trend. The KWW relaxation function is calculated by using the $M''(\omega)$ spectra, as[90]

$$\phi(t) = \frac{2}{\pi}\int_0^\infty \left(\frac{M''(\omega)}{\omega M_\infty}\right)\cos(\omega t)\mathrm{d}\omega \quad (24)$$

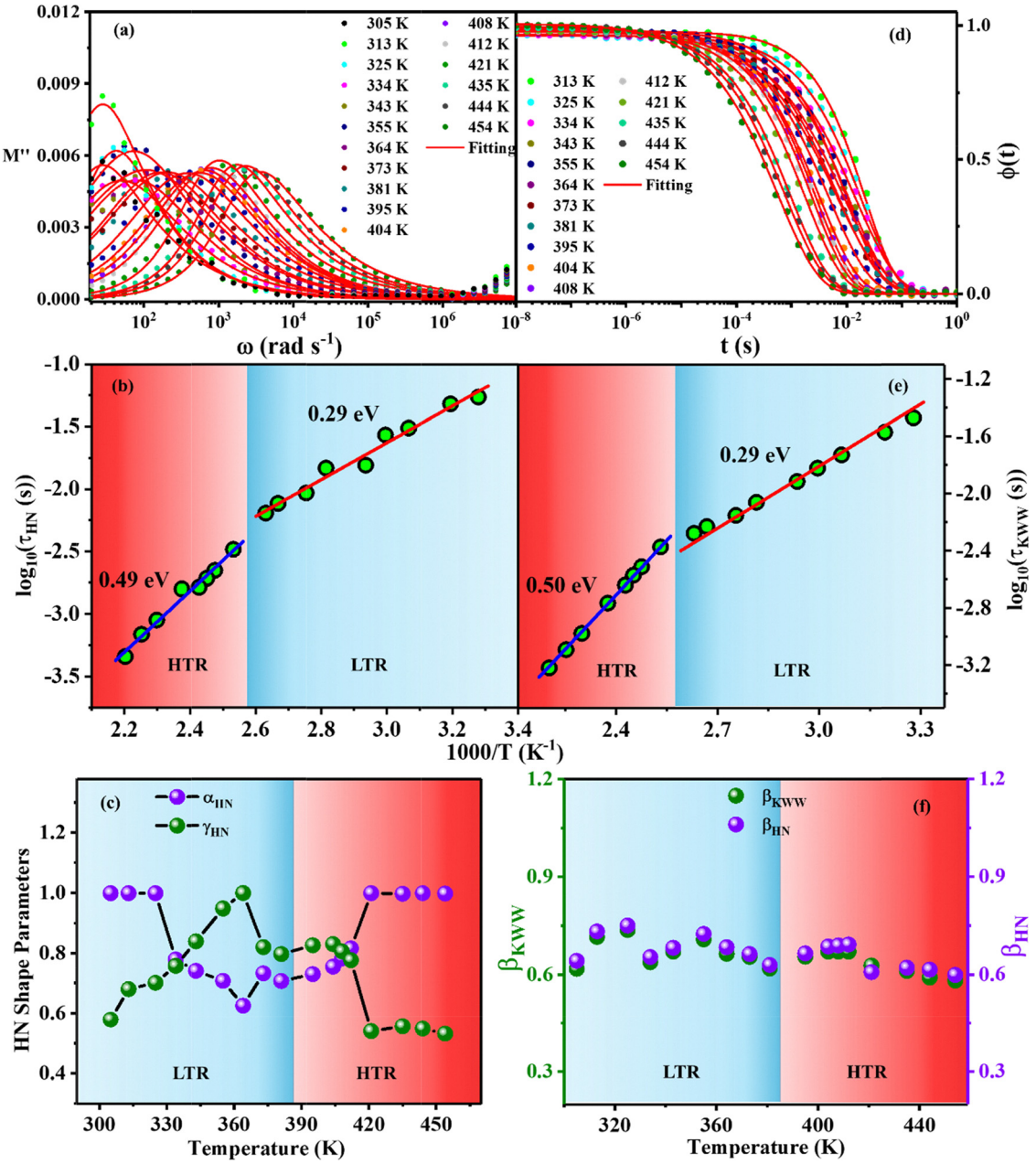

Fig. 6 (a) Electric modulus loss spectra fitted using the Havriliak–Negami (HN) model at different temperatures (305–454 K), (b) Arrhenius plot of relaxation time obtained from the HN fit and (c) temperature dependence of the HN-shape parameters, (d) time-domain analysis of electric modulus loss spectra by the KWW relaxation function at different temperatures (305–454 K), (e) Arrhenius plot of KWW relaxation time *vs.* inverse temperature, and (f) compliance of relation between the HN and KWW fitting parameters.

which is the inverse Fourier transformation of the complex electric modulus, $M^*(\omega)$, represented in the following form[87]

$$M^*(\omega) = M_\infty\left(1 - \int_0^\infty \left(-\frac{\mathrm{d}\phi}{\mathrm{d}t}\right)\mathrm{e}^{-j\omega t}\mathrm{d}t\right) \qquad (25)$$

The KWW relaxation function for the $FAPbBr_2I$ perovskite in the temperature range 305–454 K was then calculated using the experimentally observed $M''(\omega)$ data in eqn (24) and fitted by the KWW relaxation function defined in eqn (23). The fitted KWW function at various temperatures is shown in Fig. 6(d). The fitting parameters, τ_{KWW} and β_{KWW}, obtained at all temperatures (305–454 K), are summarized in Table SIV in the ESI.† The KWW relaxation time also obeys the Arrhenius relation: $\tau_{KWW} = \tau_0 \exp\left(\frac{E_{KWW}}{k_B T}\right)$ with the inverse temperature. The Arrhenius plot of the KWW relaxation time, shown in Fig. 6(e), also demonstrated the two activation energies, E_{KWW1} = 0.29 ± 0.05 eV and E_{KWW2} = 0.50 ± 0.05 eV in the LTR and HTR, respectively, further corroborating the values of AE of hopping migration obtained from the hopping frequency Arrhenius plot in both temperature regimes. Furthermore, we also verified the compliance of fitting the observed electric

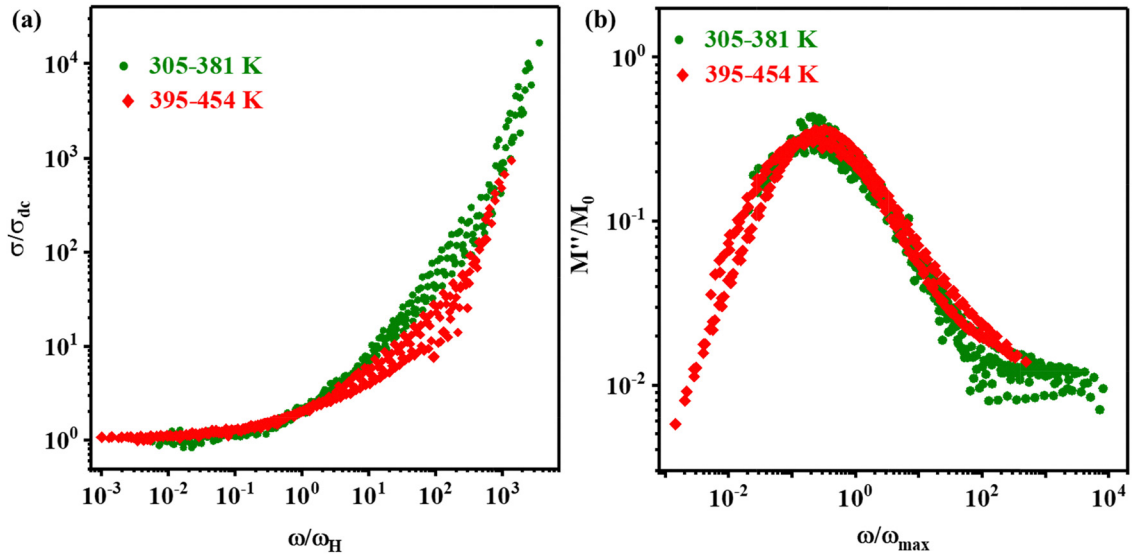

Fig. 7 Scaling of (a) AC conductivity and (b) electric modulus loss spectra of the $FAPbBr_2I$ perovskite at different temperatures.

modulus data at various temperatures using both the HN and KWW formalisms. For this, the parameters of both HN and KWW models must obey the following relation:[88]

$$(\alpha_{HN}\gamma_{HN})^{\frac{1}{1.23}} = \beta_{KWW} \quad (26)$$

The plotted values of both β_{KWW} and β_{HN} *vs.* T are shown in Fig. 6(f) and demonstrate the compliance of KWW and HN in fitting the CEM spectra.

The scaling process of a physical quantity is employed to probe whether the dynamical processes associated with that quantity are affected by the external parameters, *viz.* temperature, composition, and others. The scaling of the AC conductivity and electric modulus loss spectra acquired at different temperatures to a master curve suggests the distinct physical mechanisms behind the ionic conduction and relaxation processes.[91] Several parameters have been previously used to scale the AC conductivity and modulus loss spectra.[91–95] For the $FAPbBr_2I$ perovskite, the temperature-dependent AC conductivity is scaled by scaling the conductivity (σ') and frequency (ω) axes by σ_{dc} and ω_H and is presented in Fig. 7(a). The electric modulus loss spectra are also scaled similarly, by scaling the modulus (M'') and frequency (ω) axes by M''_{max} and ω_{max} respectively, as displayed in Fig. 7(b). The AC conductivity scaling plot (Fig. 7(a)) performed using the Pan and Ghosh model[95] depicts a common master curve in the LTR (305–381 K, shown by green scatter plots), and a slightly different master-curve at the HTR (395–454 K, shown by red scatter plots). Additionally, the scaling plot of modulus loss spectra (Fig. 7(b)) also shows slightly different master curves in the LTR and HTR. The scaling of σ_{dc} and ω_H thus are also indicative of two different ionic conduction and hopping relaxation mechanisms in the low-temperature and the high-temperature regimes.

IV. Conclusions

In summary, we have grown single crystals of FA-based mixed halide $FAPbBr_2I$ using the inverse temperature crystallization method. The structural and optical characterization was performed using XRD and UV-vis techniques. The XRD analysis rendered the cubic crystal structure of $FAPbBr_2I$ with the $Pm\bar{3}m$ space group. The ion conduction and relaxation dynamics at different temperatures (305–454 K) were probed by complex impedance spectroscopy, complex electric modulus spectroscopy, and AC conductivity. These spectra were analyzed using various theoretical models, *viz.* the Maxwell–Wagner equivalent circuit model, Havriliak–Negami (HN) and Kohlrausch–Williams–Watts (KWW) model, and modified Jonscher power law. The Nyquist plots obtained from the fits to the Maxwell–Wagner model were used to interpret the contributions of grains and grain boundaries to the total impedance. The HN model and JPL confirmed the presence of two regions of ionic conductivity. In the LTR (305–381 K), we observed almost similar values of AE of ionic conduction and hopping migration ($E_a = E_m = 0.30 \pm 0.05$ eV) since the temperature response of ionic conduction in this temperature range is dependent only on the hopping frequency. On the other hand, in the HTR, we observed a substantial increase in the number of mobile ions, facilitated by overcoming an activation energy barrier, $E_f = 0.24 \pm 0.05$ eV of forming mobile ions, as evidenced by the differences in activation energies ($E_a = 0.74 \pm 0.05$ eV and $E_m = 0.50 \pm 0.05$ eV). The temperature-dependent SCLC measurements on the Ag/$FAPbBr_2I$ SC/Ag device revealed that these mobile ions can significantly influence the nature of steady-state *J–V* characteristics and reaffirm the role of traps and mobile ions in understanding the observed thermally activated mechanism of ionic conduction and hopping migration. Lastly, the temperature scaling of the AC conductivity and complex electric modulus also validates the existence of different conduction and hopping mechanisms in low-temperature and high-temperature regions.

Conflicts of interest

There are no conflicts to declare.

Data availability

The data supporting this article have been included as part of the ESI.†

Acknowledgements

Funding from the ANRF, Government of India, under Project No. CRG/2022/005258 is gratefully acknowledged. We also thank the Central Instrumentation Facility at IIT Gandhinagar for facilitating several measurements. We also acknowledge Mr Surya Pratap Singh Shekhawat from the Department of Applied Physics in Delhi Technological University for facilitating the impedance measurements.

References

1 R. Su, Z. Xu, J. Wu, D. Luo, Q. Hu, W. Yang, X. Yang, R. Zhang, H. Yu and T. P. Russell, Dielectric screening in perovskite photovoltaics, *Nat. Commun.*, 2021, **12**(1), 2479.
2 J. N. Wilson, J. M. Frost, S. K. Wallace and A. Walsh, Dielectric and ferroic properties of metal halide perovskites, *APL Mater.*, 2019, **7**(1), 010901.
3 Y. He, M. Petryk, Z. Liu, D. G. Chica, I. Hadar, C. Leak, W. Ke, I. Spanopoulos, W. Lin and D. Y. Chung, $CsPbBr_3$ perovskite detectors with 1.4% energy resolution for high-energy γ-rays, *Nat. Photonics*, 2021, **15**(1), 36–42.
4 Z. Li, F. Zhou, H. Yao, Z. Ci, Z. Yang and Z. Jin, Halide perovskites for high-performance X-ray detector, *Mater. Today*, 2021, **48**, 155–175.
5 W.-J. Yin, J.-H. Yang, J. Kang, Y. Yan and S.-H. Wei, Halide perovskite materials for solar cells: a theoretical review, *J. Mater. Chem. A*, 2015, **3**(17), 8926–8942.
6 R. Ding, X. Zhang, G. Chen, H. Wang, R. Kishor, J. Xiao, F. Gao, K. Zeng, X. Chen and X. W. Sun, High-performance piezoelectric nanogenerators composed of formamidinium lead halide perovskite nanoparticles and poly (vinylidene fluoride), *Nano Energy*, 2017, **37**, 126–135.
7 W. Yu, F. Li, L. Yu, M. R. Niazi, Y. Zou, D. Corzo, A. Basu, C. Ma, S. Dey and M. L. Tietze, Single crystal hybrid perovskite field-effect transistors, *Nat. Commun.*, 2018, **9**(1), 5354.
8 T. Paul, P. K. Sarkar, S. Maiti, A. Sahoo and K. K. Chattopadhyay, Solution-processed light-induced multilevel non-volatile wearable memory device based on $CsPb_2Br_5$ perovskite, *Dalton Trans.*, 2022, **51**(10), 3864–3874.
9 M. Singh, J. Nama, T. Paul, N. H. Makani, A. Sahoo, S. Sharma and R. Banerjee, Photoelectrochemically Induced CO_2 Reduction Using Halide-Tunable Lead-Free Perovskites, *ACS Appl. Energy Mater.*, 2023, **6**(6), 3566–3578.
10 T. Paul, A. Sahoo, S. Maiti, D. S. Gavali, R. Thapa and R. Banerjee, Halide Tunablility Leads to Enhanced Biomechanical Energy Harvesting in Lead-Free Cs_2SnX_6-PVDF Composites, *ACS Appl. Mater. Interfaces*, 2023, **15**(29), 34726–34741.
11 A. Sahoo, T. Paul, A. Nath, S. Maiti, P. Kumar, P. Ghosh and R. Banerjee, Preferential Perovskite Surface-termination Induced High Piezoresponse in Lead-free *in situ* Fabricated $Cs_3Bi_2Br_9$-PVDF Nanocomposites Promotes Biomechanical Energy Harvesting, *Nanoscale*, 2023, **15**(27), 11603–11615.
12 A. Sahoo, T. Paul, N. H. Makani, S. Maiti and R. Banerjee, High piezoresponse in low-dimensional inorganic halide perovskite for mechanical energy harvesting, *Sustainable Energy Fuels*, 2022, **6**(19), 4484–4497.
13 T. M. Brenner, D. A. Egger, L. Kronik, G. Hodes and D. Cahen, Hybrid organic—inorganic perovskites: low-cost semiconductors with intriguing charge-transport properties, *Nat. Rev. Mater.*, 2016, **1**(1), 1–16.
14 Q. Dong, Y. Fang, Y. Shao, P. Mulligan, J. Qiu, L. Cao and J. Huang, Electron-hole diffusion lengths > 175 μm in solution-grown $CH_3NH_3PbI_3$ single crystals, *Science*, 2015, **347**(6225), 967–970.
15 C. M. Sutter-Fella, Y. Li, M. Amani, J. W. Ager III, F. M. Toma, E. Yablonovitch, I. D. Sharp and A. Javey, High photoluminescence quantum yield in band gap tunable bromide containing mixed halide perovskites, *Nano Lett.*, 2016, **16**(1), 800–806.
16 P. Basumatary and P. Agarwal, A short review on progress in perovskite solar cells, *Mater. Res. Bull.*, 2022, **149**, 111700.
17 R. Kumar, P. Srivastava, T. Kumar and M. Bag, Electronic-Ionic Transport in MAPbBr3 Single Crystal: The Evidence of Super-Linear Power Law in AC Conductivity, *J. Phys. Chem. C*, 2022, **126**(33), 14305–14311.
18 Y. Lei, Y. Chen and S. Xu, Single-crystal halide perovskites: opportunities and challenges, *Matter*, 2021, **4**(7), 2266–2308.
19 Y. Cho, H. R. Jung and W. Jo, Halide perovskite single crystals: growth, characterization, and stability for optoelectronic applications, *Nanoscale*, 2022, **14**(26), 9248–9277.
20 H. Jiang and C. Kloc, Single-crystal growth of organic semiconductors, *MRS Bull.*, 2013, **38**(1), 28–33.
21 M. I. Saidaminov, A. L. Abdelhady, B. Murali, E. Alarousu, V. M. Burlakov, W. Peng, I. Dursun, L. Wang, Y. He and G. Maculan, High-quality bulk hybrid perovskite single crystals within minutes by inverse temperature crystallization, *Nat. Commun.*, 2015, **6**(1), 7586.
22 D. Shi, V. Adinolfi, R. Comin, M. Yuan, E. Alarousu, A. Buin, Y. Chen, S. Hoogland, A. Rothenberger and K. Katsiev, Low trap-state density and long carrier diffusion in organolead trihalide perovskite single crystals, *Science*, 2015, **347**(6221), 519–522.
23 Y. Dang, Y. Liu, Y. Sun, D. Yuan, X. Liu, W. Lu, G. Liu, H. Xia and X. Tao, Bulk crystal growth of hybrid perovskite material $CH_3NH_3PbI_3$, *CrystEngComm*, 2015, **17**(3), 665–670.
24 D. P. McMeekin, G. Sadoughi, W. Rehman, G. E. Eperon, M. Saliba, M. T. Hörantner, A. Haghighirad, N. Sakai, L. Korte and B. Rech, A mixed-cation lead mixed-halide perovskite absorber for tandem solar cells, *Science*, 2016, **351**(6269), 151–155.
25 R. Gupta, V. Gupta, R. Datt, S. Arya, A. Pandey, A. Singh, S. Husale, R. Srivastava and S. Pathak, Enhanced photosensitive properties of a single-crystal formamidinium lead

bromide iodine ($FAPbBr_2I$) based photodetector, *Mater. Adv.*, 2022, **3**(4), 2089–2095.
26 K. Sekar, R. Manisekaran, O. M. Nwakanma and M. Babudurai, Significance of Formamidinium Incorporation in Perovskite Composition and Its Impact on Solar Cell Efficiency: A Mini-Review, *Adv. Energy Sustainability Res.*, 2024, **5**(8), 2400003.
27 M. Li, R. Sun, J. Chang, J. Dong, Q. Tian, H. Wang, Z. Li, P. Yang, H. Shi and C. Yang, Orientated crystallization of FA-based perovskite via hydrogen-bonded polymer network for efficient and stable solar cells, *Nat. Commun.*, 2023, **14**(1), 573.
28 S. Sidhik, I. Metcalf, W. Li, T. Kodalle, C. J. Dolan, M. Khalili, J. Hou, F. Mandani, A. Torma and H. Zhang, Two-dimensional perovskite templates for durable, efficient formamidinium perovskite solar cells, *Science*, 2024, **384**(6701), 1227–1235.
29 M. Que, Y. Li, H. Yuan, P. Zhong, B. Li, J. Wei, P. Hu, L. Gao, W. Huang and S. Liu, Surface Doping to Suppress Iodine Ion Migration for Stable $FAPbI_3$ Perovskite Quantum Dot Solar Cells, *Small*, 2025, **21**(4), 2406569.
30 J. Kim, J. S. Park, G. Y. Kim and W. Jo, Autonomous Control of Ion Migration at α-$FAPbI_3$ Heterointerfaces *via* Interfacial-Self-Assembled 2D Perovskite, *Adv. Energy Mater.*, 2024, **14**(40), 2402117.
31 Y. Liang, F. Li, X. Cui, T. Lv, C. Stampfl, S. P. Ringer, X. Yang, J. Huang and R. Zheng, Toward stabilization of formamidinium lead iodide perovskites by defect control and composition engineering, *Nat. Commun.*, 2024, **15**(1), 1707.
32 D. K. LaFollette, J. Hidalgo, O. Allam, J. Yang, A. Shoemaker, R. Li, B. Lai, B. Lawrie, S. Kalinin and C. A. Perini, Bromine Incorporation Affects Phase Transformations and Thermal Stability of Lead Halide Perovskites, *J. Am. Chem. Soc.*, 2024, **146**(27), 18576–18585.
33 O. Nazarenko, S. Yakunin, V. Morad, I. Cherniukh and M. V. Kovalenko, Single crystals of caesium formamidinium lead halide perovskites: solution growth and gamma dosimetry, *NPG Asia Mater.*, 2017, **9**(4), e373.
34 L. Chen, Y.-Y. Tan, Z.-X. Chen, T. Wang, S. Hu, Z.-A. Nan, L.-Q. Xie, Y. Hui, J.-X. Huang and C. Zhan, Toward long-term stability: single-crystal alloys of cesium-containing mixed cation and mixed halide perovskite, *J. Am. Chem. Soc.*, 2019, **141**(4), 1665–1671.
35 J. Berry, T. Buonassisi, D. A. Egger, G. Hodes, L. Kronik, Y. L. Loo, I. Lubomirsky, S. R. Marder, Y. Mastai and J. S. Miller, Hybrid organic–inorganic perovskites (HOIPs): Opportunities and challenges, *Adv. Mater.*, 2015, **27**(35), 5102–5112.
36 D. Ghosh, E. Welch, A. J. Neukirch, A. Zakhidov and S. Tretiak, Polarons in halide perovskites: a perspective, *J. Phys. Chem. Lett.*, 2020, **11**(9), 3271–3286.
37 N. H. Makani, A. Sahoo, P. Pal, T. Paul, L. S. Tanwar, M. Singh, A. Ghosh and R. Banerjee, Onset of vacancy-mediated high activation energy leads to large ionic conductivity in two-dimensional layered $Cs_2PbI_2Cl_2$ Ruddlesden–Popper halide perovskite, *Phys. Rev. Mater.*, 2022, **6**(11), 115002.
38 C. G. Bischak, C. L. Hetherington, H. Wu, S. Aloni, D. F. Ogletree, D. T. Limmer and N. S. Ginsberg, Origin of reversible photoinduced phase separation in hybrid perovskites, *Nano Lett.*, 2017, **17**(2), 1028–1033.
39 W. Tress, Metal Halide Perovskites as Mixed Electronic–Ionic Conductors: Challenges and Opportunities□ From Hysteresis to Memristivity, *J. Phys. Chem. Lett.*, 2017, **8**(13), 3106–3114.
40 N. K. Tailor, N. Parikh, P. Yadav and S. Satapathi, Dielectric Relaxation and Polaron Hopping in $Cs_2AgBiBr_6$ Halide Double Perovskites, *J. Phys. Chem. C*, 2022, **126**(24), 10199–10208.
41 G. Y. Kim, A. Senocrate, T.-Y. Yang, G. Gregori, M. Grätzel and J. Maier, Large tunable photoeffect on ion conduction in halide perovskites and implications for photodecomposition, *Nat. Mater.*, 2018, **17**(5), 445–449.
42 L.-C. Chen, K.-L. Lee, C.-H. Tien and H.-Y. Wei, $FAPbBr_{3-x}I_x$ perovskite quantum dots red Light-Emitting diodes with double confinement layer structure, *Mater. Sci. Eng.: B*, 2021, **264**, 114969.
43 R. Ding, H. Liu, X. Zhang, J. Xiao, R. Kishor, H. Sun, B. Zhu, G. Chen, F. Gao and X. Feng, Flexible piezoelectric nanocomposite generators based on formamidinium lead halide perovskite nanoparticles, *Adv. Funct. Mater.*, 2016, **26**(42), 7708–7716.
44 M. A. Afroz, C. A. Aranda, N. K. Tailor, Yukta, P. Yadav, M. M. Tavakoli, M. Saliba and S. Satapathi, Impedance spectroscopy for metal halide perovskite single crystals: Recent advances, challenges, and solutions, *ACS Energy Lett.*, 2021, **6**(9), 3275–3286.
45 M. Singh, T. Paul, P. Pal, A. Sahoo, L. S. Tanwar, N. H. Makani, A. Ghosh and R. Banerjee, High ionic conduction and polarity-induced piezoresponse in layered bimetallic $Rb_4Ag_2BiBr_9$ single crystals, *J. Phys. Chem. C*, 2022, **126**(51), 21810–21824.
46 M. Sajedi Alvar, P. W. Blom and G. J. A. Wetzelaer, Device model for methylammonium lead iodide perovskite with experimentally validated ion dynamics, *Adv. Electron. Mater.*, 2020, **6**(6), 1900935.
47 F. Borsa, D. Torgeson, S. W. Martin and H. K. Patel, Relaxation and fluctuations in glassy fast-ion conductors: wide-frequency-range NMR and conductivity measurements, *Phys. Rev. B: Condens. Matter Mater. Phys.*, 1992, **46**(2), 795.
48 M. E. Hajlaoui, R. Dhahri, N. Hnainia, A. Benchaabane, E. Dhahri and K. Khirouni, Conductivity and giant permittivity study of $Zn_{0.5}Ni_{0.5}Fe_2O_4$ spinel ferrite as a function of frequency and temperature, *RSC Adv.*, 2019, **9**(56), 32395–32402.
49 A. Guerrero, J. Bisquert and G. Garcia-Belmonte, Impedance spectroscopy of metal halide perovskite solar cells from the perspective of equivalent circuits, *Chem. Rev.*, 2021, **121**(23), 14430–14484.
50 S. Govinda, B. P. Kore, D. Swain, A. Hossain, C. De, T. N. Guru Row and D. Sarma, Critical comparison of $FAPbX_3$ and $MAPbX_3$ (X = Br and Cl): how do they differ?, *J. Phys. Chem. C*, 2018, **122**(25), 13758–13766.
51 S. Govinda, B. P. Kore, M. Bokdam, P. Mahale, A. Kumar, S. Pal, B. Bhattacharyya, J. Lahnsteiner, G. Kresse and C. Franchini, Behavior of methylammonium dipoles in $MAPbX_3$ (X = Br and I), *J. Phys. Chem. Lett.*, 2017, **8**(17), 4113–4121.
52 D. Gets, G. Verkhogliadov, E. Danilovskiy, A. Baranov, S. Makarov and A. Zakhidov, Dipolar cation accumulation

at the interfaces of perovskite light-emitting solar cells, *J. Mater. Chem. C*, 2020, **8**(47), 16992–16999.
53 D. Singh, K. Shahi and K. K. Kar, Superlinear frequency dependence of AC conductivity and its scaling behavior in xAgI-$(1-x)$ $AgPO_3$ glass superionic conductors, *Solid State Ionics*, 2016, **287**, 89–96.
54 A. K. Jonscher, The 'universal'dielectric response, *Nature*, 1977, **267**(5613), 673–679.
55 C. Koops, On the dispersion of resistivity and dielectric constant of some semiconductors at audiofrequencies, *Phys. Rev.*, 1951, **83**(1), 121.
56 D. Almond and A. West, Anomalous conductivity prefactors in fast ion conductors, *Nature*, 1983, **306**(5942), 456–457.
57 X. Zheng, S. Wang, J. Wang, W. Hua, J. Zhang and L. Liu, Long-range and short-range transport dynamics of Li ions in $LiMn_2O_4$, *J. Phys. Chem. C*, 2020, **124**(46), 25254–25261.
58 K. Funke and R. Hoppe, Jump-relaxation model yields Kohlrausch-Williams-Watts behaviour, *Solid State Ionics*, 1990, **40**, 200–204.
59 S. Yang, S. Y. Kim and G. Chen, Halide Superionic Conductors for All-Solid-State Batteries: Effects of Synthesis and Composition on Lithium-Ion Conductivity, *ACS Energy Lett.*, 2024, **9**(5), 2212–2221.
60 D. Almond, G. Duncan and A. West, The determination of hopping rates and carrier concentrations in ionic conductors by a new analysis of ac conductivity, *Solid State Ionics*, 1983, **8**(2), 159–164.
61 H. Jin, E. Debroye, M. Keshavarz, I. G. Scheblykin, M. B. Roeffaers, J. Hofkens and J. A. Steele, It's a trap! On the nature of localised states and charge trapping in lead halide perovskites, *Mater. Horiz.*, 2020, **7**(2), 397–410.
62 D. Meggiolaro, E. Mosconi and F. De Angelis, Formation of surface defects dominates ion migration in lead-halide perovskites, *ACS Energy Lett.*, 2019, **4**(3), 779–785.
63 C. León, K. Ngai and A. Rivera, Correlation between ion hopping conductivity and near constant loss in ionic conductors, *Phys. Rev. B: Condens. Matter Mater. Phys.*, 2004, **69**(13), 134303.
64 A. Rivera, C. León, J. Sanz, J. Santamaria, C. Moynihan and K. Ngai, Crossover from ionic hopping to nearly constant loss in the fast ionic conductor $Li_{0.18}La_{0.61}TiO_3$, *Phys. Rev. B: Condens. Matter Mater. Phys.*, 2002, **65**(22), 224302.
65 A. Senocrate, I. Moudrakovski, G. Y. Kim, T. Y. Yang, G. Gregori, M. Grätzel and J. Maier, The nature of ion conduction in methylammonium lead iodide: a multi-method approach, *Angew. Chem.*, 2017, **129**(27), 7863–7867.
66 M. H. Futscher, J. M. Lee, L. McGovern, L. A. Muscarella, T. Wang, M. I. Haider, A. Fakharuddin, L. Schmidt-Mende and B. Ehrler, Quantification of ion migration in $CH_3NH_3PbI_3$ perovskite solar cells by transient capacitance measurements, *Mater. Horiz.*, 2019, **6**(7), 1497–1503.
67 T. Shi, H.-S. Zhang, W. Meng, Q. Teng, M. Liu, X. Yang, Y. Yan, H.-L. Yip and Y.-J. Zhao, Effects of organic cations on the defect physics of tin halide perovskites, *J. Mater. Chem. A*, 2017, **5**(29), 15124–15129.
68 D. J. Kubicki, D. Prochowicz, E. Salager, A. Rakhmatullin, C. P. Grey, L. Emsley and S. D. Stranks, Local structure and dynamics in methylammonium, formamidinium, and cesium tin(II) mixed-halide perovskites from ^{119}Sn solid-state NMR, *J. Am. Chem. Soc.*, 2020, **142**(17), 7813–7826.
69 A. Pockett, G. E. Eperon, N. Sakai, H. J. Snaith, L. M. Peter and P. J. Cameron, Microseconds, milliseconds and seconds: deconvoluting the dynamic behaviour of planar perovskite solar cells, *Phys. Chem. Chem. Phys.*, 2017, **19**(8), 5959–5970.
70 W. Li, M. U. Rothmann, Y. Zhu, W. Chen, C. Yang, Y. Yuan, Y. Y. Choo, X. Wen, Y.-B. Cheng and U. Bach, The critical role of composition-dependent intragrain planar defects in the performance of $MA_{1-x}FA_xPbI_3$ perovskite solar cells, *Nat. Energy*, 2021, **6**(6), 624–632.
71 Q. Zhang, X. Liu, X. Zhang, Z. Wang, B. Zhang, Y. Hao, A. Dubois, W. Jie and Y. Xu, Single nucleation of Cl-doped $FAPbBr_3$ with inhibited ion migration for ambipolar radiation detection, *J. Mater. Chem. A*, 2024, **12**(6), 3304–3310.
72 A. Oranskaia, J. Yin, O. M. Bakr, J.-L. Brédas and O. F. Mohammed, Halogen migration in hybrid perovskites: the organic cation matters, *J. Phys. Chem. Lett.*, 2018, **9**(18), 5474–5480.
73 S. Rizvi, P. Mantri and B. Mazhari, Traps signature in steady state current-voltage characteristics of organic diode, *J. Appl. Phys.*, 2014, **115**(24), 244502.
74 J. A. Röhr, T. Kirchartz and J. Nelson, On the correct interpretation of the low voltage regime in intrinsic single-carrier devices, *J. Phys.: Condens. Matter*, 2017, **29**(20), 205901.
75 E. A. Duijnstee, J. M. Ball, V. M. Le Corre, L. J. A. Koster, H. J. Snaith and J. Lim, Toward understanding space-charge limited current measurements on metal halide perovskites, *ACS Energy Lett.*, 2020, **5**(2), 376–384.
76 N. R. W. Mott *Gurney Electronic Processes in ionic crystals*, Clarendon, Oxford, 1948, vol. 12, p. 155.
77 M. A. Lampert, Simplified theory of space-charge-limited currents in an insulator with traps, *Phys. Rev.*, 1956, **103**(6), 1648.
78 A. Stoneham, *Current Injection in Solids*, IOP Publishing, 1970.
79 E. A. Duijnstee, V. M. Le Corre, M. B. Johnston, L. J. A. Koster, J. Lim and H. J. Snaith, Understanding dark current-voltage characteristics in metal-halide perovskite single crystals, *Phys. Rev. Appl.*, 2021, **15**(1), 014006.
80 V. M. Le Corre, E. A. Duijnstee, O. El Tambouli, J. M. Ball, H. J. Snaith, J. Lim and L. J. A. Koster, Revealing charge carrier mobility and defect densities in metal halide perovskites *via* space-charge-limited current measurements, *ACS Energy Lett.*, 2021, **6**(3), 1087–1094.
81 M. Sajedi Alvar, P. W. Blom and G.-J. A. Wetzelaer, Space-charge-limited electron and hole currents in hybrid organic-inorganic perovskites, *Nat. Commun.*, 2020, **11**(1), 4023.
82 F. Tian and Y. Ohki, Electric modulus powerful tool for analyzing dielectric behavior, *IEEE Trans. Dielectr. Electr. Insul.*, 2014, **21**(3), 929–931.
83 Y. Ohki, Broadband complex permittivity and electric modulus spectra for dielectric materials research, *IEEJ Trans. Electr. Electron. Eng.*, 2022, **17**(7), 958–972.
84 S. Havriliak and S. Negami, A complex plane representation of dielectric and mechanical relaxation processes in some polymers, *Polymer*, 1967, **8**, 161–210.

85 P. Pal and A. Ghosh, Ionic conduction and relaxation mechanisms in three-dimensional $CsPbCl_3$ perovskite, *J. Appl. Phys.*, 2021, **129**(23), 234102.
86 F. Kohlrausch Kohlrausch, *Poggendorff's Ann. Phys.*, 1863, **119**, 352.
87 G. Williams and D. C. Watts, Non-symmetrical dielectric relaxation behaviour arising from a simple empirical decay function, *Trans. Faraday Soc.*, 1970, **66**, 80–85.
88 F. Alvarez, A. Alegra and J. Colmenero, Relationship between the time-domain Kohlrausch-Williams-Watts and frequency-domain Havriliak-Negami relaxation functions, *Phys. Rev. B: Condens. Matter Mater. Phys.*, 1991, **44**(14), 7306.
89 A. Lukichev, Relaxation function for the non-Debye relaxation spectra description, *Chem. Phys.*, 2014, **428**, 29–33.
90 F. Howell, R. Bose, P. Macedo and C. Moynihan, Electrical relaxation in a glass-forming molten salt, *J. Phys. Chem.*, 1974, **78**(6), 639–648.
91 B. Roling, A. Happe, K. Funke and M. Ingram, Carrier concentrations and relaxation spectroscopy: new information from scaling properties of conductivity spectra in ionically conducting glasses, *Phys. Rev. Lett.*, 1997, **78**(11), 2160.
92 S. Summerfield, Universal low-frequency behaviour in the ac hopping conductivity of disordered systems, *Philos. Mag. B*, 1985, **52**(1), 9–22.
93 N. Balkan, P. Butcher, W. Hogg, A. Long and S. Summerfield, Analysis of frequency-dependent loss data in amorphous silicon and germanium, *Philos. Mag. B*, 1985, **51**(1), L7–L12.
94 T. B. Schrøder and J. C. Dyre, Scaling and universality of ac conduction in disordered solids, *Phys. Rev. Lett.*, 2000, **84**(2), 310.
95 A. Ghosh and A. Pan, Scaling of the conductivity spectra in ionic glasses: dependence on the structure, *Phys. Rev. Lett.*, 2000, **84**(10), 2188.

